# Far-infrared observations of normal stars measured with ISOPHOT in mini-map mode

Attila Moór, Péter Ábrahám, Csaba Kiss, Szilárd Csizmadia

Konkoly Observatory, Budapest, Hungary
19-June-2003

Version 1.1

## 1 Introduction and General Principles

The release of the final version of the ISOPHOT Off-Line Processing software (OLP V10.0) and the generation of the ISO Legacy Archive closed the main period of ISOPHOT calibration. In this phase the calibration work focused on general instrumental effects with impact on several or all observing modes, and the correction algorithms developed were as general as possible in order to ease the software implementation. The photometric quality reached with the OLP is documented in the Scientific Validation Report Richards & Klaas (2002) and in the ISOPHOT Calibration Accuracies Document Klaas et al. (2002).

In a very general calibration approach, however, specific problems of individual observing modes (or submodes) might be overlooked or ignored. In order to improve further the photometric accuracy of ISOPHOT our strategy is to carry out more specific calibration investigations focusing on particular problems of well-defined homogeneous data sets, and to work out dedicated correction algorithms which are not necessarily applicable to other data sets. We adopt the following general scheme for the analysis of a selected well-defined ISOPHOT observing mode or submode:

1. Collect from the Archive all observations performed in the selected observing mode;
2. Identify all objects which can be used as secondary photometric standards;
3. Process the measurements of identified standard objects using an OLP V10-compatible data reduction method;
4. Search for any systematic trend in the (Measured-Predicted) residual flux densities;
5. Investigate the physical reason behind of the observed trend, invent new data processing methods to eliminate it and reprocess the data with the new methods;
6. Repeat Points 4-5 until all understandable physical reasons are eliminated;
7. In case a residual trend is still present in the data, fit the trend and invent an empirical formula to correct for the systematic discrepancies;
8. Document the new processing methods and the empirical fits;

As a first project we started a re-evaluation of all ISOPHOT observations obtained in the so-called mini-map mode. In this report we describe our product, a catalogue of all normal stars observed in mini-map mode. These results will be made available to the public as Highly Processed Data Products in the ISO Data Archive.

# 2 Establishment of secondary standards for ISOPHOT photometric calibration

## 2.1 Motivation

As described in Sect.1, it is a fundamental point of our calibration strategy to supplement the relatively short list of official photometric standards with science observations of targets with predictable fluxes. This would be extremely important at very low flux levels. Our favoured objects for this purpose are stars. In this section we describe our methods to predict flux densitites at far-infrared wavelengths for normal stars.

## 2.2 Prediction of fluxes for the ISOPHOT bandpass central wavelengths

### 2.2.1 Models for the primary ISOPHOT calibration sources

The photometric system of ISOPHOT is defined by a homogeneous set of 197 photospheric templates/models of 157 normal stars produced by M. Cohen and P. Hammersley. Of this collection 24 stars were actually used at $\lambda \leq 25\mu$m and twelve ones at longer wavelengths. In order to extend the calibration to higher fluxes also asteroids (Müller & Lagerros (2002)) and planets (Griffin & Orton) were involved. In Appendix A we list the 157 standard stars, whose models were downloaded from the homepage of the ISO Data Centre, together with their spectral types and $BV$ photometries taken from the Hipparcos catalogue. The stars actually used for ISOPHOT calibration are marked.

### 2.2.2 Colours of normal stars in the ISOPHOT bandpass central wavelengths

In order to predict flux densities at the ISOPHOT central wavelengths for our newly added secondary standards, first we predict the monochromatic colour-corrected flux density of a star for a selected reference wavelength. This reference wavelength can be arbitrarily chosen; we selected $\lambda = 25\mu m$ because the majority of the Cohen models are not calculated beyond $35\mu m$.

How to do this prediction will be discussed in details in the next subsections. In the second step we compute the flux densities at other ISOPHOT bandpass central wavelength by multiplying the prediction at $25\mu m$ by the $F_\nu(\lambda)/F_\nu(25\mu m)$ infrared 'colour'.

In the present study we consider only stars, and their infrared colours are almost constant, apart from a slight systematic variation with the spectral type. In order to characterize this variation the $F_\nu(\lambda)/F_\nu(25\mu m)$ ratios were computed from the standard models. Our results demonstrate that after correcting for the variations with spectral type the remaining scatter is almost negligible, therefore, once the flux density at 25 micron is known the fluxes in other filters can be predicted with high accuracy.

### 2.2.3 Prediction of the $25\mu$m photospheric flux of normal stars from the K-magnitude

In this subsection we investigate the prediction the flux density of a normal star at 25 micron from its $K$-magnitude and $B-V$ optical colour.

A long list of normal stars was observed at near-infrared wavelengths in the framework of the ISO Ground Based Preparatory Programme (GBPP). The observations were performed either in Tenerife (Telescopio "Carlos Sánchez", TCS) or at La Silla (ESO). For the stars listed in Appendix A we extracted the model flux density at $25\mu m$, converted it into magnitudes $[25]$, and computed the $K-[25]$ magnitude difference. For this conversion we adopted the formula

$$[25] = -2.5 \times \lg[F_{25}/F^0_{25}] \quad (1)$$

where $F^0_{25}$ is the flux density corresponding to 0 magnitude (following IRAS we adopted $F^0_{25} = 6.73$Jy). In Fig. 1 these $K-[25]$ values are plotted versus the optical B-V colours. Considering only stars observed with TCS (the majority of the cases) we fitted the distribution with a 4th order polynomial:

$$[25] = K_{(TCS)} - (a + b(B-V) + c(B-V)^2 + d(B-V)^3 + e(B-V)^4) \quad (2)$$

where

$$a = -0.0830573$$
$$b = -6.09696 \times 10^{-7}$$
$$c = 0.122921$$
$$d = 2.90976 \times 10^{-7}$$
$$e = -0.0148661$$

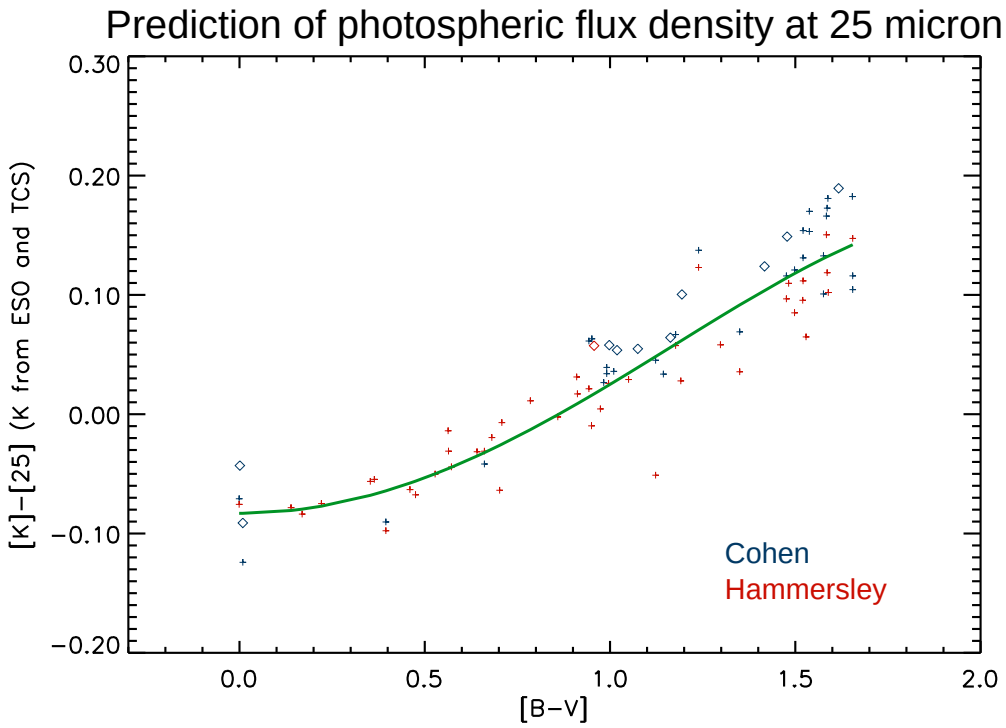


Figure 1: Prediction of the 25 micron flux density via fitting the [K-25] vs. [B-V] relationship for standard stars. The K magnitudes are from ESA and TCS photometry, the $25\mu m$ magnitudes are from predictions by Cohen and Hammersley. The B-V magnitudes are from Hipparcos (Appendix A).

The conversion from magnitude to flux density at 25 micron is:

$$F_{25} = 6.73 \times 10.0^{-0.4 \cdot [25]} \text{ Jy} \quad (3)$$

Figure 2 shows the consistency check of this method. For all stars measured with TCS we calculated the $25\mu m$ flux density according to formulae (1)-(3) and compared the result with their model values at 25 micron. The standard deviation of the ratio predicted/model flux indicates, that, if a $K$-band measurement with TCS is available, the $25\mu m$ flux density for a normal star can be predicted with an $1\sigma$ accuracy of 2.5%.

$K$-band measurements obtained at other telescopes have to be transferred to the TCS photometric system. Below we give the transformation between the ESO and the TCS photometric systems derived from our data:

$$K_{(TCS)} = K_{(ESO)} + (a + bK_{(ESO)} + cK^2_{(ESO)}) \quad (4)$$

where

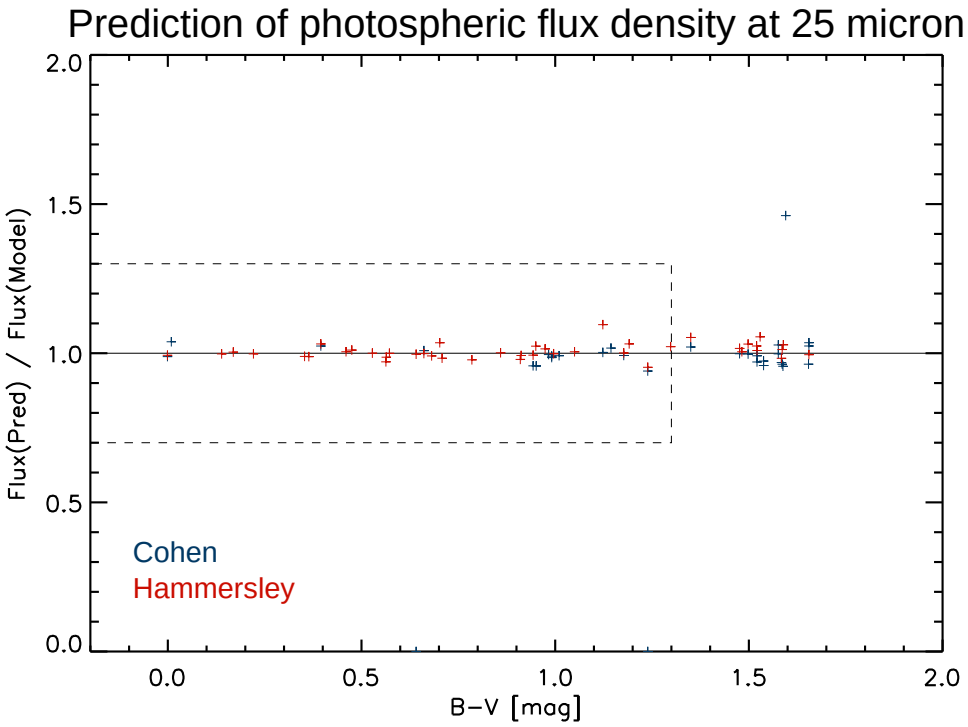


Figure 2: Consistency check of our method predicting the 25 micron flux density of the Cohen/Hammersley stars from the K-magnitude and the [B-V] colour index. The 1 $\sigma$ standard deviation of the predicted-to-model flux ratio is 2.5% at B-V $< 1.3$.

$$a = -0.0458388$$
$$b = -0.00409587$$
$$c = 0.000558516$$

The 2MASS All Sky Catalogue was published in April, 2003. It provides good quality $J$, $H$ and $K$ data for the whole sky. In order to use 2MASS $K$-magnitudes to predict the far-infrared flux densities of stars we have to determine the transformation of 2MASS $K$-magnitudes into the TCS-system. 585 stars were found which are included in both catalogues, and their study yielded the following relation:

$$K_{TCS} = 0.993(\pm 0.002) K_{2MASS} + 0.041(\pm 0.011) \quad (5)$$

The transformation has no significant colour-term according to our analyses:

$$K_{TCS} = K_{2MASS} + 0.002(\pm 0.004)(J-K)_{2MASS} + 0.007(\pm 0.009) \quad (6)$$

Since the slope of the (2) transformation equation is not significant, we will use only an magnitude offset which was determined as the median value of the individual deviations between the two systems. Its value was found to be $-0.007$ magnitude relative to the TCS system.

Note that the bright stars ($K <\sim 4.5$ magnitude) in the 2MASS $JHK$ catalogue have a high error (more than 10%). This is probable a consequence of their saturation and due to this effect we did not include these bright stars in our analyses. Therefore the transformation is valid only for $4.5 < K < 10.0$ magnitude.

In the case of data coming from other telescopes one should check if a transformation into the TCS photometric system is necessary. The formulae above make it possible to predict the 25 micron flux density with an accuracy of 2-3% for stars observed either with TCS, ESO and 2MASS.

### 2.2.4 Prediction of the photospheric $25\mu m$ flux of normal stars from the V-magnitude

Because some stars may not have K-band observations in this subsection we investigate the possibility of predicting the $25\mu m$ flux density from the $V$-magnitude and the $B-V$ colour, in a way similar to the one described in the previous subsection. Procedures like this were already worked out for IRAS data (see e.g. Plets & Vynckier (1999)). Figure 3 shows the $V-[25]$ vs. $[B-V]$ relationship for the ISO primary standard stars (Appendix A). As V-magnitudes we adopted the Johnson magnitudes $V(J)$ from the Hipparcos catalogue. The data can well be fitted with the 3rd order formula used by Laureijs (2000), but only the input $25\mu m$ fluxes are divided by a factor of 1.07:

$$[25] = V - (0.01 + 2.99(B-V) - 1.06(B-V)^2 + 0.47(B-V)^3) \tag{7}$$

$$F_{25} = 6.73 \times 10.0^{-0.4\cdot[25]}\ \mathrm{Jy} \tag{8}$$

$$F_{25} = \frac{F_{25}}{1.07} \tag{9}$$

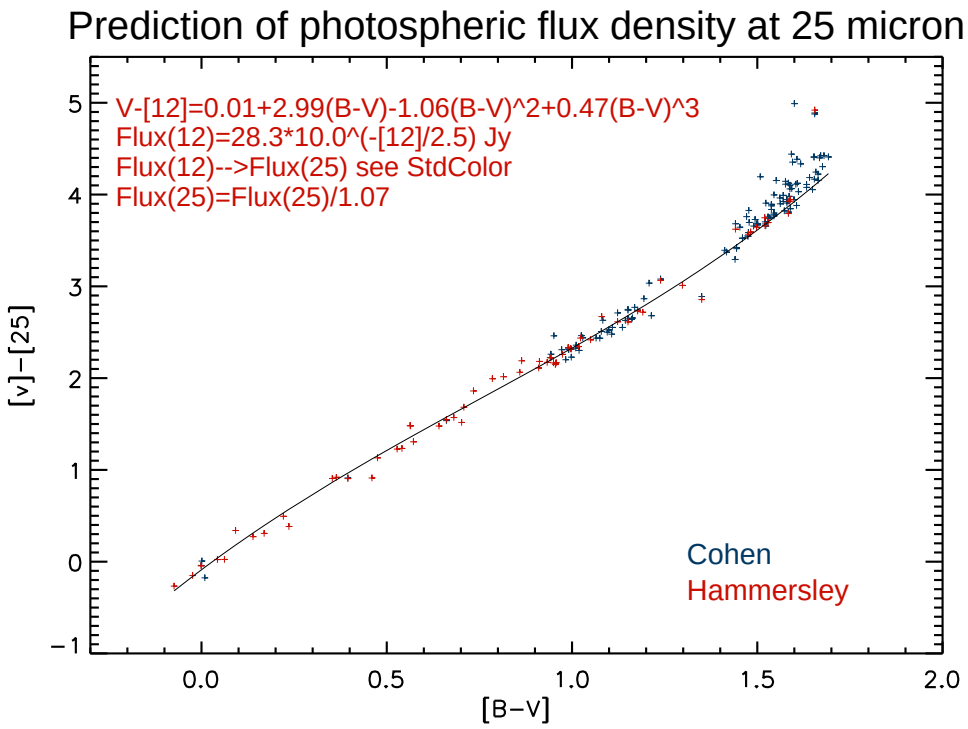


Figure 3: Prediction of the 25 micron flux density via fitting the [V-25] vs. [B-V] relationship for all standard stars provided by Cohen/Hammersley.

Figure 4 shows the consistency check. For each primary standard star we calculated the $25\mu m$ flux density from its Johnson $V$-magnitude and $B-V$ optical colour using the formulae above, and compared the result with its model flux at 25 micron. Although in general a good agreement was found, at $B-V > 1.3$ (M-type stars) the scatter increases significantly. For $B-V < 1.3$ (A-K type stars) the standard deviation of the predicted-to-model flux is 8%, three times worse than the one obtained from the $K$-magnitudes.

In the present study we predicted the flux densities according to the following priority sequence:

1. Cohen/Hammersley model (see Appendix A) ;
2. prediction from K magnitudes (TCS, ESO, 2MASS) and B-V optical colour;

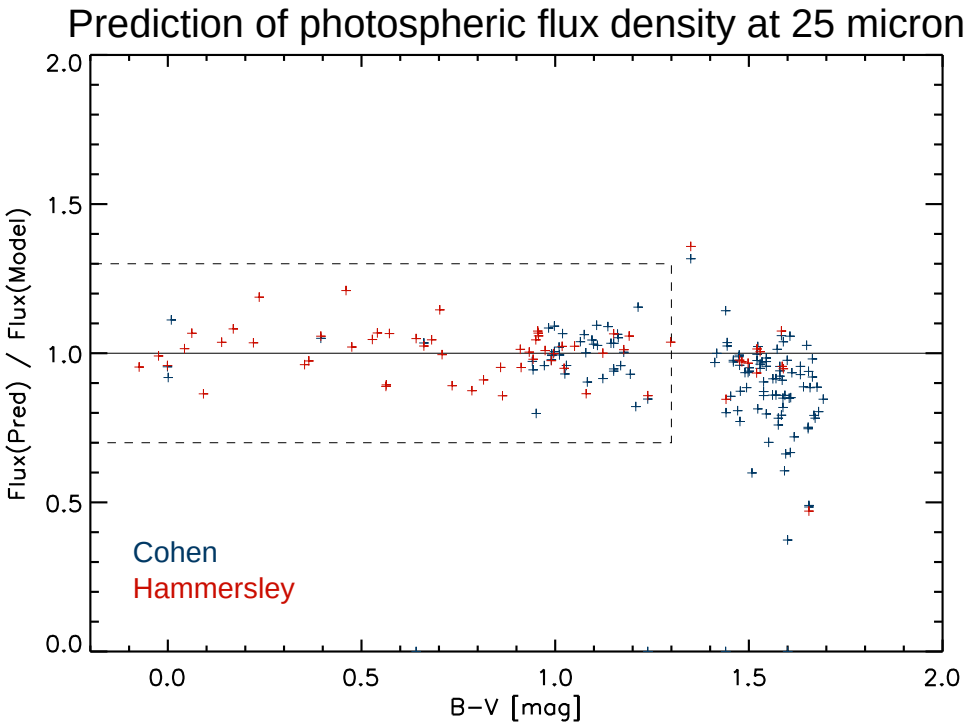


Figure 4: Consistency check of our method predicting the 25 micron flux density from the V-magnitude and the [B-V] colour index. The standard deviation at $B - V < 1.3$ (A–K stars) is 8%.

3. prediction from Johnson V magnitudes and B-V optical colour;

# 3 The ISOPHOT mini-map mode

## 3.1 Definition of the mini-map mode

The mini-map mode was one of the most efficient ways of obtaining poin source photometry with the C100 and C200 detectors. It was also the mode used for FCS calibration observations.

C100 mini-maps are typically 3x3 raster maps performed in satellite coordinate system centered on the source. In the recommended and most frequently used configuration $\Delta M = \Delta N = 46''$ (one detector pixel) in combination with an odd number of raster steps in both directions.

Figure 5 presents a typical road map of a 3x3 C100 mini-map, outlying how the detector pixels observe the source one by one. At the first raster step the source illuminates pixel 7, at the next step the source illuminates pixel 4 and at the last step it illuminates pixel 3.

Due to the fact that the target position is observed by all 9 detector pixels, the C100 minimaps have several advantages:

1. rather than relying only on the pixel 5 calibration, the final photometry is a combination of 9 independently calibrated flux density values;
2. the observational efficiency is very high, because e.g. in a 3x3 minimap the target is continuously measured during the full length of the observation by one of the detector pixels;

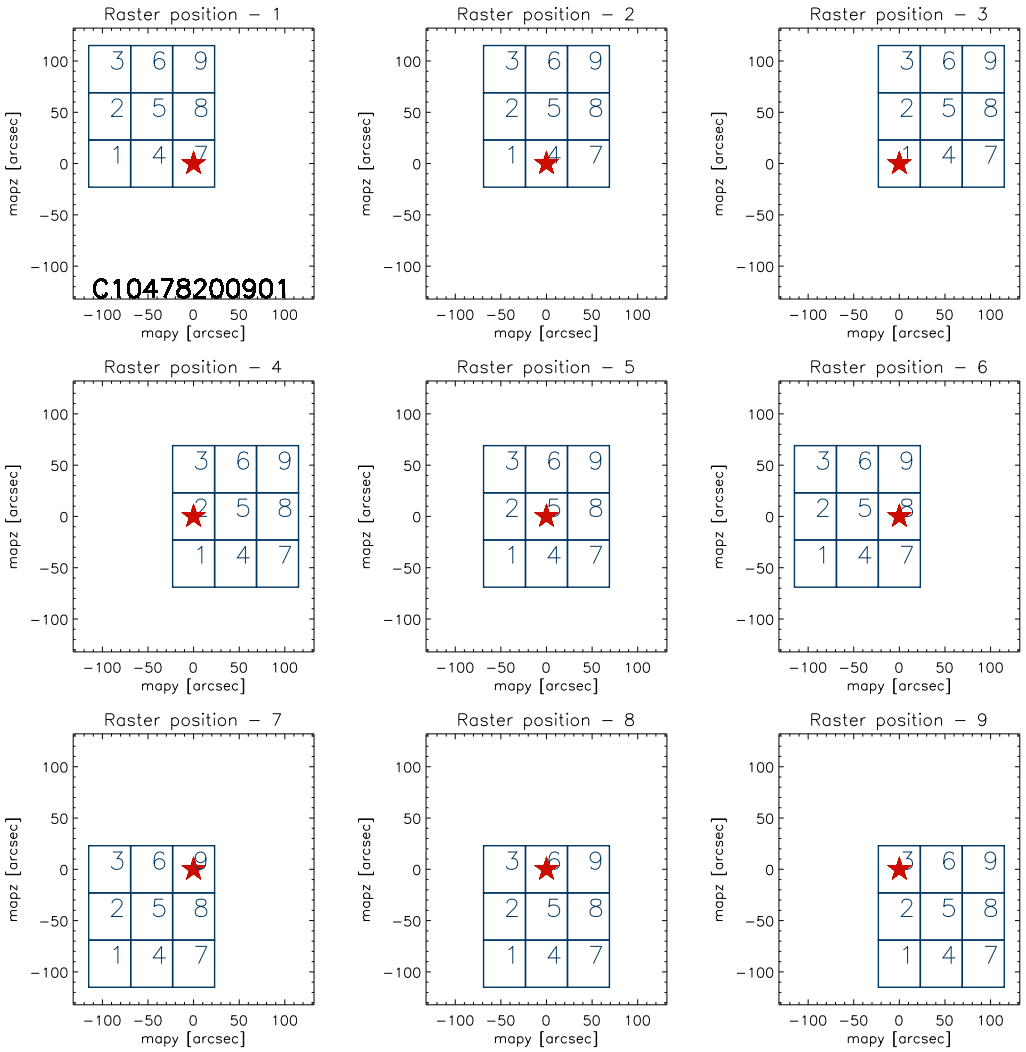


Figure 5: The position of the pixels of the C100 detector with regard to the source for the different raster positions along a 3x3 raster scan centered on the source

For the C200 detector the usual configuration was $\Delta M = \Delta N = 92''$ together with an even number of raster steps. Similarly to the C100 case, the observing efficiency is high, and each of the 4 detector pixels provide an independent flux density. An extra advantage over C200 staring measurements is that the source is observed at the centre of the detector pixels rather than at the centre of the array (which is located on gaps between the pixels), increasing the signal to noise.

Minimaps performed in the raster mode of the PHT22 AOT were the recommended observing mode for faint point sources since August 1997. Quite a number of special calibration observations performed in the non-standard AOT mode PHT99 make use of the same raster scan technique.

## 3.2 Statistics on mini-maps in the Archive

The IDA contains 1527 mini-map observations (TDTs), selected by the following criteria:

- AOT P22 and P99 rasters with raster step numbers of $2 \geq \mathrm{M} \leq 7$ and $2 \geq \mathrm{N} \leq 7$;

- raster step sizes in the range to $45'' \pm 2''$ for C100, and $45'' \pm 2''$ or $91'' \pm 2$ in the case of the C200 detector.

It should be noted that several mini-map measurements in different filters may be associated with the same TDT number.

On the basis of the proposal keywords one can roughly classify observations into the following categories:

- calibration observations (298 TDT numbers);
- normal stars (424);
- other stellar sources (123);
- extragalactic objects (552);
- miscellaneous objects (130).

# 4 Data-base of normal star observations in mini-map mode

In order to select stars to be used as secondary standards in the following analyses we checked manually each individual mini-map in the Archive. In the first round stars included in the Cohen-Hammersley database (26 stars) were taken. The target types of the remaining mini-maps were determined by consulting SIMBAD and the proposal abstract. Stars with spectral type B-K and luminosity class IV-V were picked up. Our final database contains 555 observations of 229 stars.

For this "normal star" database we collected the following data: $K$ magnitudes (GBPP), $V$ magnitudes (Johnson V), $B - V$ indices (Tycho B-V), distances and cluster membership. Following the scheme described in Sect. 2, we predicted the flux density for the nominal wavelength of the ISOPHOT observations (in case the object was included in Cohen-Hammersley database we used the original photospheric model flux rather than the prediction).

# 5 Processing scheme

## 5.1 ERD→AAP processing with PIA v10.0

From the ERD to the AAP level the data were processed in batch mode with the PHOT Interactive Analysis software V10.0 (Gabriel et al. (1997)).

Table 1 outlines steps at the subsequent processing levels. Our processing differs from a standard reduction in the following steps:

1. We applied the new dynamic transient correction developed recently in a joint project of the ISOPHOT Data Centre at MPIA and the Konkoly Observatory. The new transient correction algorithm, not implemented in PIA V10, was available as a separate IDL code. This new method fits the temporal signal evolution within a measurement by interpolating within a library of signal dependent transient curves and predicts the signal at t = 128s (for details see del Burgo et al. (2002)). The transient correction was applied after the reset interval correction at the SRD level.
2. In case of C100 mini-map observations we used the biweight mean method (implemented as a general option in PIA V10.0, which can be used instead of the default weighted mean method) to combine the signals at SRD level because of its beneficial characteristics.

Since each mini-map is bracketed by two FCS measurements, there are several possibilities how to combine the two responsivity values. We tested, if only the second FCS measurement or a combination of the two FCS measurements (average or interpolate the responsivities in time for each raster position) gives the best photometric result. The test revealed that the two combination methods provide better results than the usage of the second FCS only. We used the averaging method to calculate the responsivities (it is the default method in PIA V10.0)

| Applied calibration and processing steps | C100 | C200 |
|---|---|---|
| **ERD** | | |
| Ramp Linearization | + | + |
| Ramp Deglitching (2threshold method) | + | + |
| **SRD** | | |
| Reset Interval Correction | + | + |
| Dynamic Transient Correction (IDL code!) | + | - |
| Dark Current Subtraction (orbit dependent) | + | + |
| Signal Linearization | + | + |
| Signal Deglitching | + | + |
| Drift recognition | - | + |
| Combine signals (SRD $\rightarrow$ SCP) | + | + |
| (bi-weight mean averaging method) | + | |
| (weighted mean averaging method) | | + |
| **SCP** | | |
| Calculate responsivities (used the average of the two FCS measurements) | + | + |
| Convert signals to monochromatic flux densities per pixel per raster position | + | + |
| **AAP** | | |

Table 1: Applied calibration and processing steps for the C100 and C200 mini-map observations at the different processing levels of PIA V10

## 5.2 Flux extraction from the AAP

### 5.2.1 Drift correction.

A mini-map measurement lasts typically 400-500 sec, and on this timescale slow baseline variations, called 'long term drift' may not be negligible. The drift is usually positive, i.e. the signal increases with time even in the case of constant illumination.

The drift introduces some uncertainty in the estimate of the background signal, and the magnitude of the effect depends on the pixel number. E.g., if the source was observed in the first raster step (Pix.7), then all off-source positions were measured at a later drift phase; thus their average gave a too high estimate for the background level towards the source. On the contrary, if the star was measured in the last raster step (Pix.3) then the average background is too low. Fig. 6 demonstrates the consequences: at low flux level Pix.7 yields source flux densities systematically too low by about 60 mJy (i.e. the subtracted background was too high), while pixels which see the source at a later phase during the drift usually have a positive offset in the source fluxes.

In order to correct for artifacts related to drift we performed a 2nd order polynomial fit to the off-source raster steps per pixel (with logarithmic scale on the time axis), and corrected the measurement according to the fit. First we determined the deviations of the fitted curve from the average flux level of the whole measurement and then subtracted this differencies from the original data points. Figure 7 shows an example. Since in the case of bright sources the off-source positions also receive some light from the source according to the footprint fraction (see Sect. 5.2.3), first we subtract the estimated contribution of the source towards each raster position. A first estimate of the source flux is determined from the intensity distribution with no drift correction. A second order fit was applied to the corrected points, and the absolute background level was scaled to the average brightness of the last three raster positions. After drift correction a new AAP file was created which can be downloaded from the HPDP set.

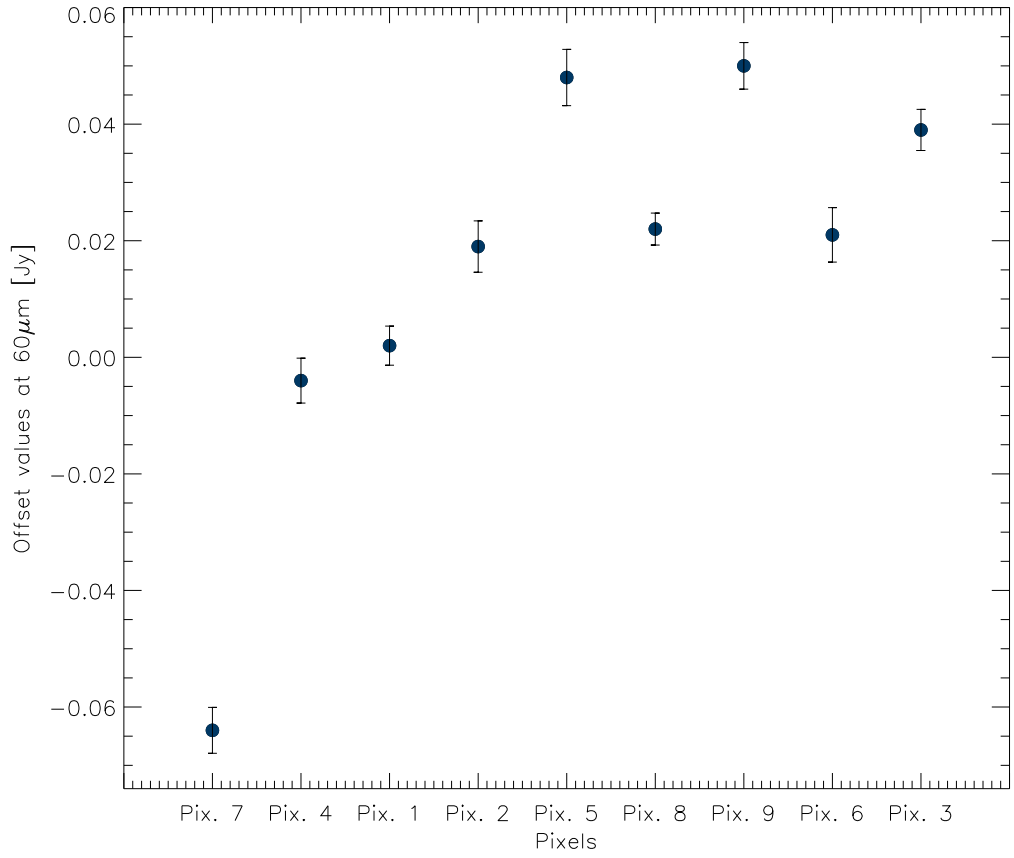


Figure 6: Average zero point offset for background subtracted (point) source fluxes for the different pixels. The pixels are ordered according to the time-sequence they observed the source

### 5.2.2 Check for point/extended nature of the object

Using dedicated high resolution observing modes it was possible to determine the diameters of several Vega-type disks with ISOPHOT (e.g. Walker H.J. & Heinrichsen I. (2000)). Although mini-maps do not count as a high resolution mode, we tested if they contain enough information to provide an estimate for the sizes of the objects. In the following we present results on the C100 detector, demonstrating ISOPHOT's capability to resolve sources of $\approx 15 - 60''$ in size.

.

Since the footprint of the C100 detector is broader than the pixel size, a small fraction of the source flux is observable on raster positions $\pm 46''$ apart. This fraction was higher if the source was extended , and comparing the measured flux fraction with a series of calibration curves created by convolving the theoretical or measured point-spread function with Gaussians of FWHM=$10''$,$20''$,$30''$,$40''$,$50''$. In a typical mini-map configuration the 9 detector pixels give altogether 24 estimates on the diameter of the source which can be averaged (assuming a radially symmetric Gaussian profile). Fig.8 presents the measured diameters for the normal stars sample. In the case of faint sources the high noise prevents any quantitative statement. Among the bright stars the two prototype Vega stars (Vega, $\alpha$PsA) are clearly extended. Assuming spherical symmetry and averaging the measurements of all pixels and all appropriate raster positions we get FWHM of $19.4''$ and $15.4''$, respectively, for the extents of the two stars. For comparison, at submillimetre wavelengths Vega was measured to be $24''$x$21''$, while $\alpha$PsA has an extent of $41''$x$18''$ (Holland et al. (1998)). The edge-on disk of $\beta$ Pic is $22''$x$11''$ at submillimetre wavelengths,

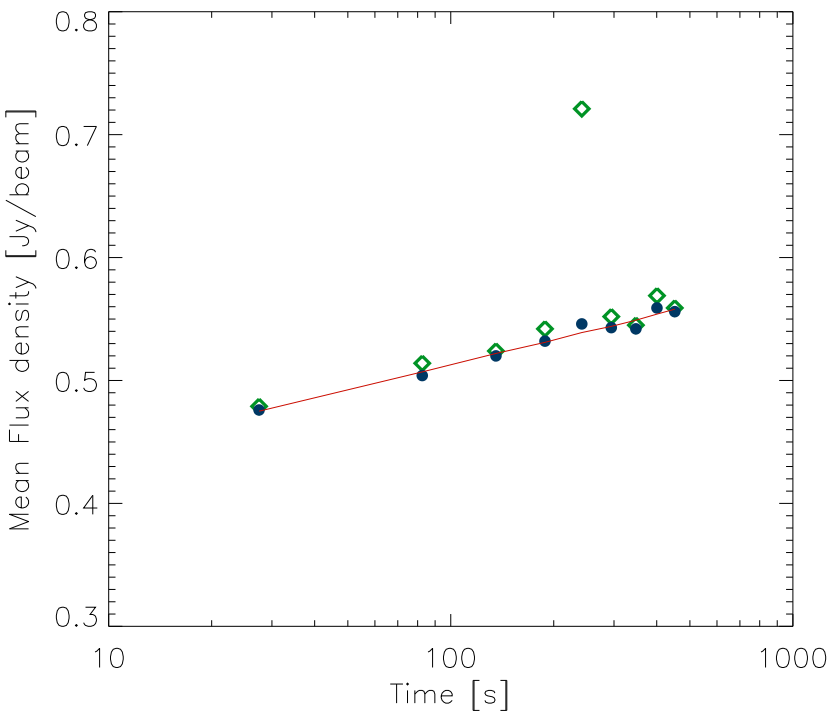


Figure 7: Example of the drift correction (for the HD8907, TDT number = 78200901, pixel 5). Open diamonds show the original data while dots mark data after subtracting the source's contribution

while only 14.5″x6.1″ at 60$\mu$m as determined from high-resolution ISOPHOT scans (Heinrichsen et al. (1999)). With our method $\beta$ Pic is not resolved showing the limitations of this technique.

### 5.2.3 Flux extraction.

In order to achieve good accuracies for point source photometry we used a modified version of the PCASPHT method (Kiss & Klaas (2000)) to extract fluxes from AAP files. The PCASPHT method is based on the determination of fluxes from the data stream of each individual pixel. Each pixel at each raster position sees a certain amount of the flux of the central (point) source, plus the background assumed to be constant at all positions:

$$I_{ij} = f_{ij} \times I_j^S + I_j^{BG}$$

Here $I_j^S$ is the total flux of the central source measured by the $j$th pixel, $I_j^{BG}$ is the constant background flux, measured by the $j$th pixel, $f_{ij}$ is the fraction of the central source flux on the $j$th pixel at the $i$th raster position and $I_{ij}$ is the measured flux on the $j$th pixel at the $i$th raster position.

Whereas the position of each pixel at each raster step is determined in image coordinates, the offsets can be calculated easily relative to the centre of the raster. Assuming that the source is at the centre of the raster the footprint fraction factor $f_{ij}$ can be determined for the given distance from the central source. In the case of the most common mini-map configuration of $\Delta$M = $\Delta$N = 46″ (C100) or $\Delta$M = $\Delta$N = 92″ (C200), $f_{ij}$ factors relative to the footprint centre have been established by Laureijs (1999). These relative footprint values were adopted by Richards & Klaas (2002) (see their Table 1), and used also in the present work. For mini-maps of non-standard raster step sizes, however, we had to generalise the PCASPHT method to work also with the full 2-dimensional theoretically predicted beam profile (Herbstmeier et al. (1998)) or with the measured beam profile.

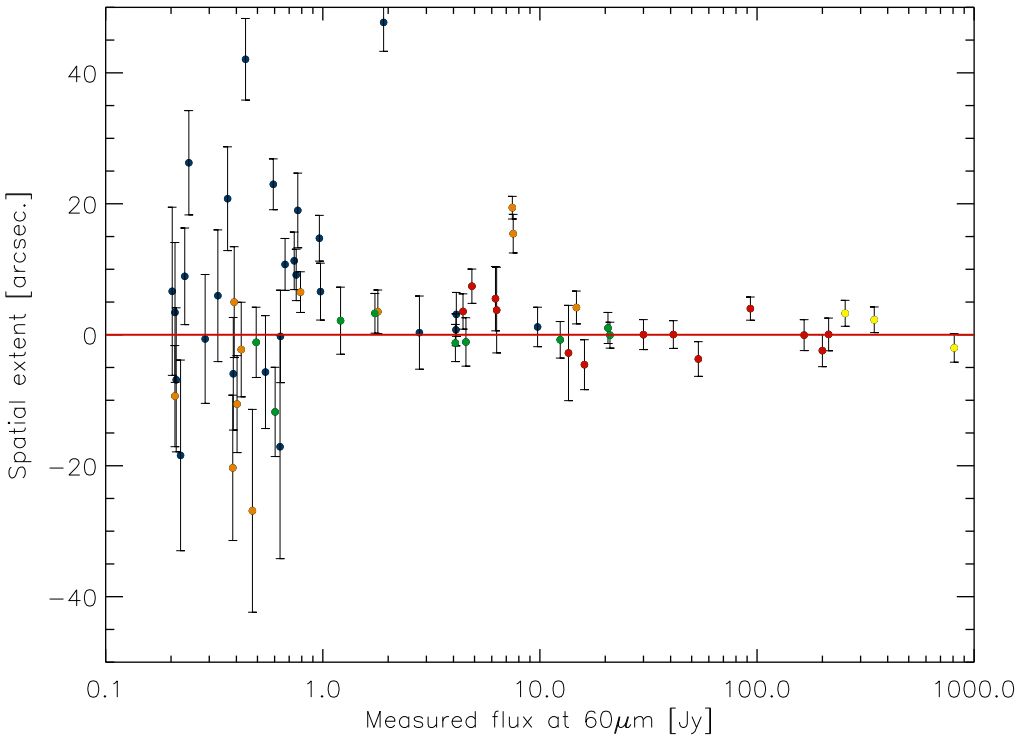


Figure 8: Spatial extent versus the measured flux densities at $60\mu m$. Orange dots : well known Vega-type stars. Blue dots: stars. Green dots: Calibration stars. Red dots: asteroids. Yellow dots: planets

In the case the source was off-centre positioned an additional uncertainty factor has to be taken into account in the general error budget.

As $I_{ij}$-s are the measured fluxes themselves, there are only two parameters to determine, $I_j^S$ and $I_j^{BG}$ for the $j$th pixel, which can be done by a simple line-fit using the $f_{ij}$-s and $I_{ij}$-s. An example is presented in Fig. 9. These kind of fits are presented for each observation/pixel in the HPDP set.

#### 5.2.4 Combine photometric results of individual pixels

In a usual C100 mini-map with the source centered on the central raster position all nine detector pixels observed the source, producing nine independent flux density values. The final source flux was derived from the average of these values. In the case of C100, after extensive systematic tests, we chose a robust averaging method called "bi-weight mean". This method, available in IDL, combines the values by assigning lower weights for outlying data points. An average background was also computed with the same method. The formal uncertainty of the source flux is also computed by the bi-weight mean routine based on a "robust sigma" algorithm. This "sigma", which is the "outlier resistant" analogue of the normal standard deviation, was divided by the square root of the number of independent flux density values.

In the case of C200 we followed a similar scheme as for C100, but the combination of the individual flux densities of the four detector pixels was performed by a weighted average. The formal flux uncertainty was also calculated by the weighted average routine.

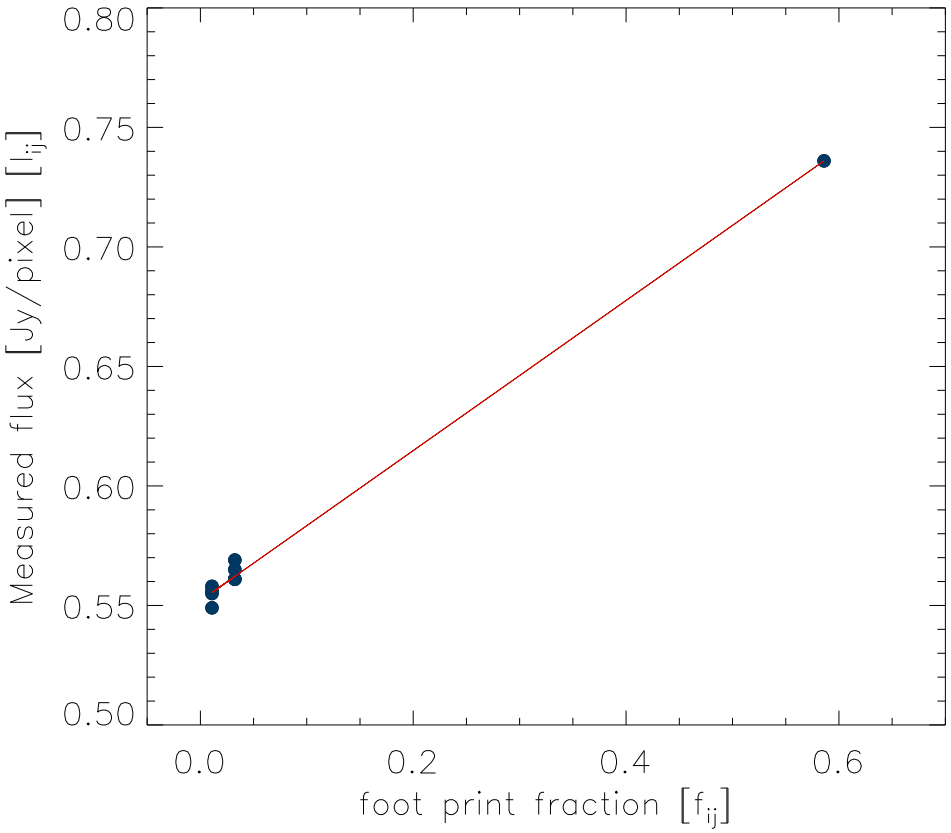


Figure 9: Example of the $I_{ij}$–$f_{ij}$ linear fit in the modified PCASPHT method (for HD8907, TDT number = 78200901, pixel 5)

## 5.3 Empirical correction for systematic trends

As a result of our improvements of the mini-map processing scheme no significant discrepancies from the predicted fluxes remained, apart from a weak systematic trend which can still be observed in the residual flux distribution. Following our general philosophy outlined in Sect. 1 we correct for this trend by means of an empirical fit. The correction curve was derived individually for each detector pixels as well as for the combined flux density.

### 5.3.1 Empirical offset correction

A comparison of the measured and predicted fluxes for the faintest sources indicate the presence of a zero point offset (see Fig. 10). In order to determine its value we selected all sources with $F_{pred} \leq 100$ mJy and calculated a robust average of the $[F_{meas} - F_{pred}]$ differences. In those filters where not enough faint observations were available the offset correction was skipped. Fig. 11 diplays the computed offset values for each pixel which are ordered according to the time sequence they observed the source in the mini-map. This figure is the counterpart of Fig. 6, and the comparison of the values in the two figures clearly demonstrate that the drift correction improved the results considerably. In order to correct for the offset we subtracted it from all measured fluxes per pixel.

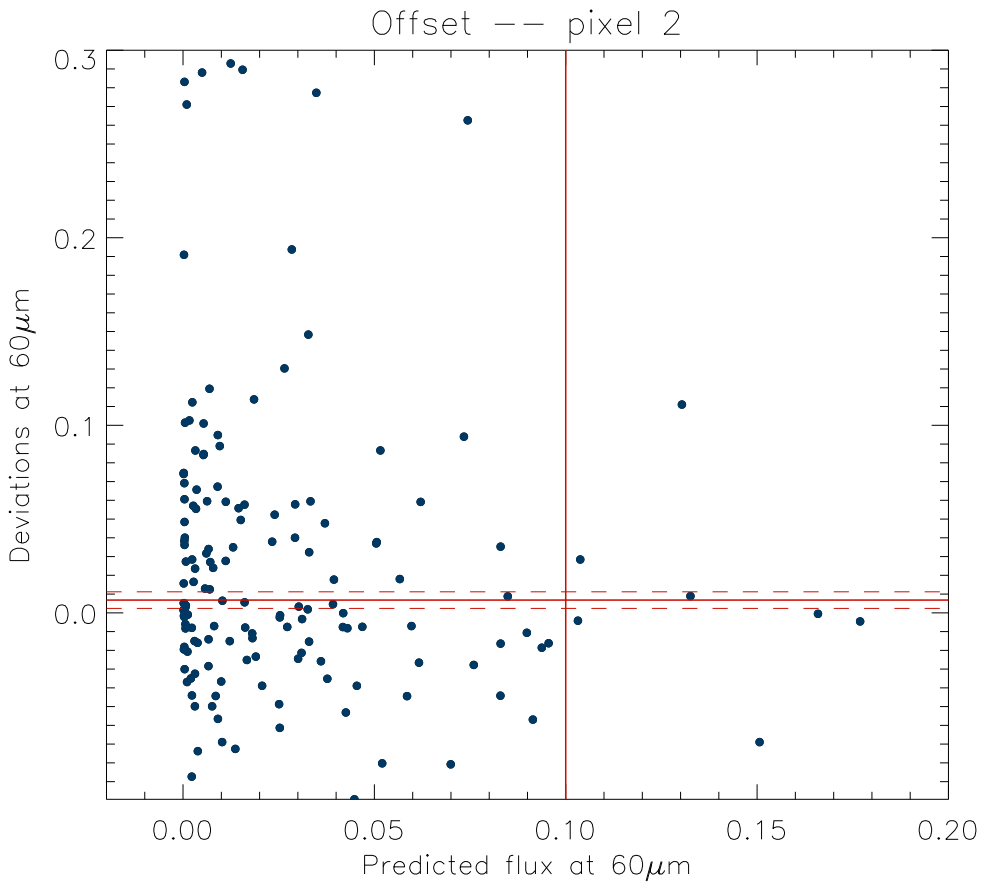


Figure 10: Determination of the zero-point offset (horizontal red line) for the faintest ($F_\nu \leq 100\mathrm{mJy}$) sources.

### 5.3.2 Empirical scaling factors

After correcting for the additive offset component all remaining differencies were assumed to be of multiplicative nature. An example for the relationship between the measured and predicted fluxes for $F_\nu > 100\mathrm{mJy}$ after offset correction is presented in Fig. 12. Firstly, the $F_{meas}/F_{pred}$ ratios were computed and plotted as a function of the predicted flux. The remaining trend around 1.0 was then fitted by a smooth curve, see Fig. 13.

In order to extend our calibration to the full dynamic range observable by ISOPHOT we included in the study several mini-map observations of bright asteroids and planets. Since at low flux level (below 100 mJy) no reliable scaling factor could be determined due to the higher noise, we requested that the fit approaches unity in this flux range. Since the official ISOPHOT standard stars have more reliable model fluxes therefore we assigned higher weights to these objects. The final flux correction was performed by dividing the measured fluxes by the fit.

# 6 Error budget

The standard deviations of the $F_{meas}$ vs. $F_{pred}$ residuals, computed after the empirical correction, were determined as follows: at low flux level a constant value independent of the source flux was assumed while at high fluxes the uncertainty was expressed as a fraction of the source's flux density, in percentage.

- At 60, 90 and 170$\mu m$ were enough faint measurements to a reliable estimate of low level constant error value. The results are 14.5, 14.5, 31.0 mJy at 60, 90 and 170$\mu m$ respectively. At 65, 80, 100, 105, 120, 150,

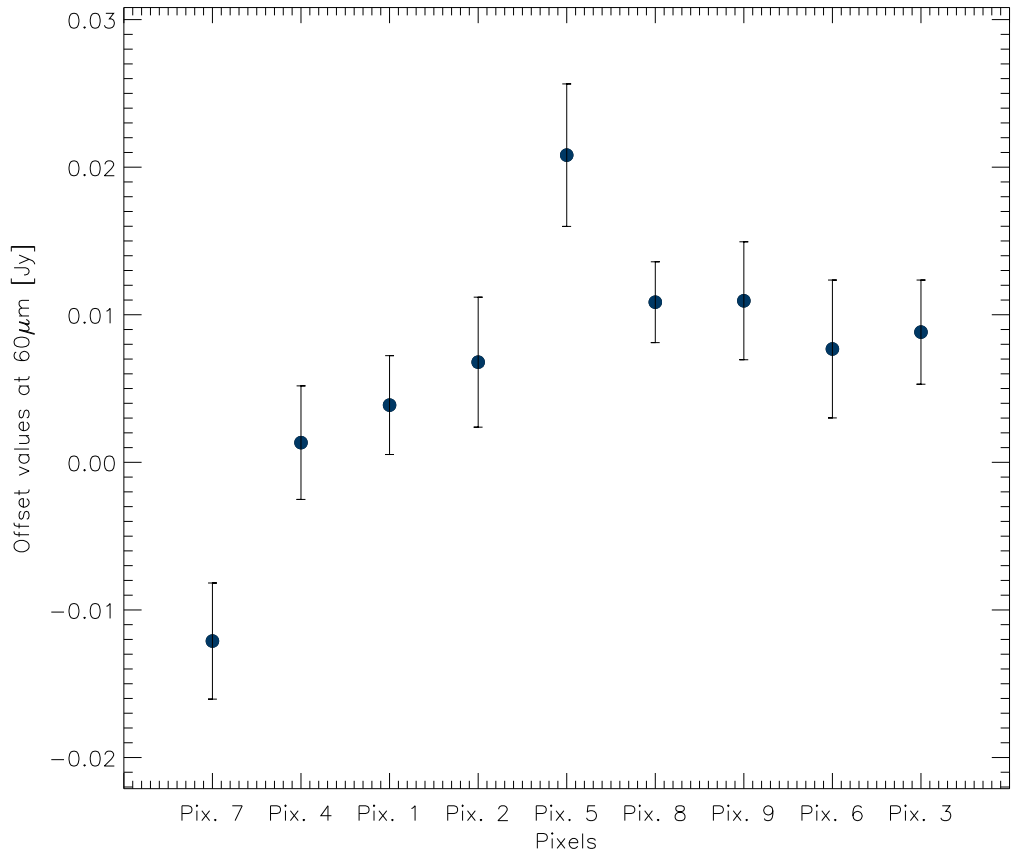


Figure 11: Same as in Fig 6 after the drift correction

180 and 200$\mu m$ the present normal star database turned out to be insufficient to determine such an error.

- The multiplicative error component, relevant for bright stars for the same three filters are: 4.0%, 7.0%, 4.5%. Asteroids and planets were not involved in this error calculation because of the higher absolute uncertainty of their model fluxes. These are the uncertainty values derived from the flux distribution of the bright star sample and the individual uncertainties may differ from it.
- In the cases of the 65, 80, 100 and 105$\mu m$ the multiplicative errors are lower than 7%.
- In the cases of the 120, 150, 180, 200$\mu m$ the multiplicative errors are lower than 9%.
- The individual error bars are computed as the standard deviation of the individual pixels' fluxes, due to the relatively low number of pixels (C100: 9 pixels, C200: 4 pixels) the derived error bar has its own statistical uncertainty. Figure 14 shows the individual error bars at 60$\mu m$ versus the background surface brightness. The point distribution suggests a weak trend with the background brightness; the scatter around this trend could partly come from this statistical uncertainty. Thus individual error bars below $\sim$ 6 mJy are unrealistic (at other wavelengths this number may be different).

We compared these uncertainty values representative of the whole database with the average of the individual error bars calculated in Sect. 5.2.4. At faint level the agreement is satisfactory for 60 and 170$\mu m$ fluxes while for 90$\mu m$ fluxes the individual error bars are lower by 40% on average. At high level the individual error bars are often systematically too low.

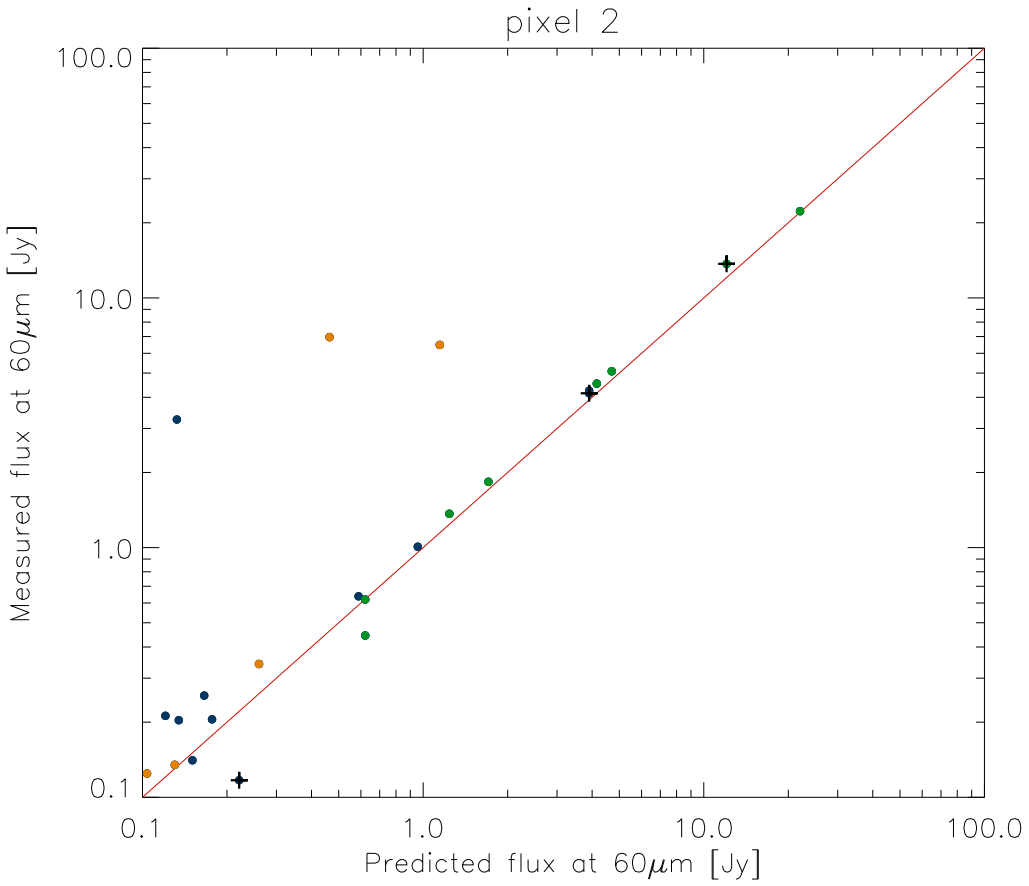


Figure 12: Measured vs. predicted flux at 60 $\mu m$ for sources of higher fluxes, where the empirical corrections is basically of multiplicative nature. Blue dots: stars. Orange dots: well known Vega-type stars. Green dots: calibration stars. Crosses: indicate measurements where the orbital phase $> 0.82$.

In order to be on the safe side we decided to modify the individual error bars. At 90$\mu m$ at low flux level the individual errors were scaled up by 40%. At high fluxes we requested the flux uncertainty never be lower than the average residual error.

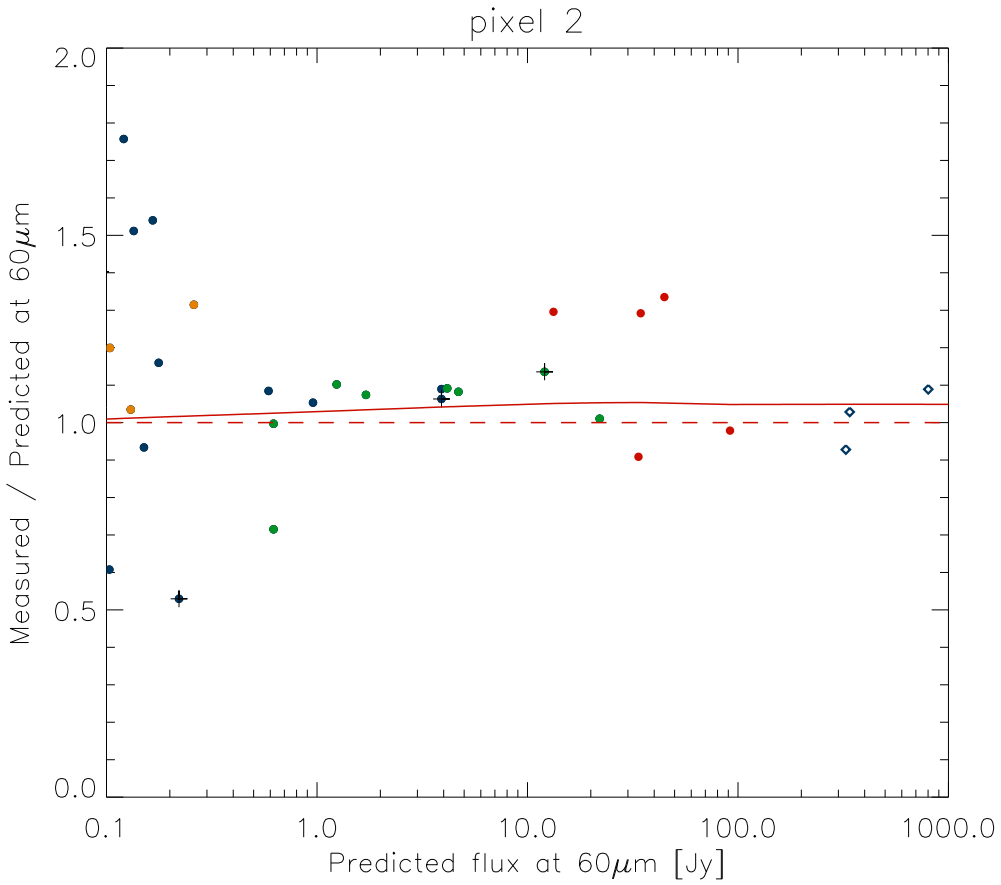


Figure 13: $F_{meas}/F_{pred}$ ratio vs. predicted flux at 60 $\mu m$.Blue dots: stars. Orange dots: well known Vega-type stars. Green dots: calibration stars. Red dots : asteroids. Blue diamonds: planets. Crosses: indicate measurements where the orbital phase $> 0.82$.

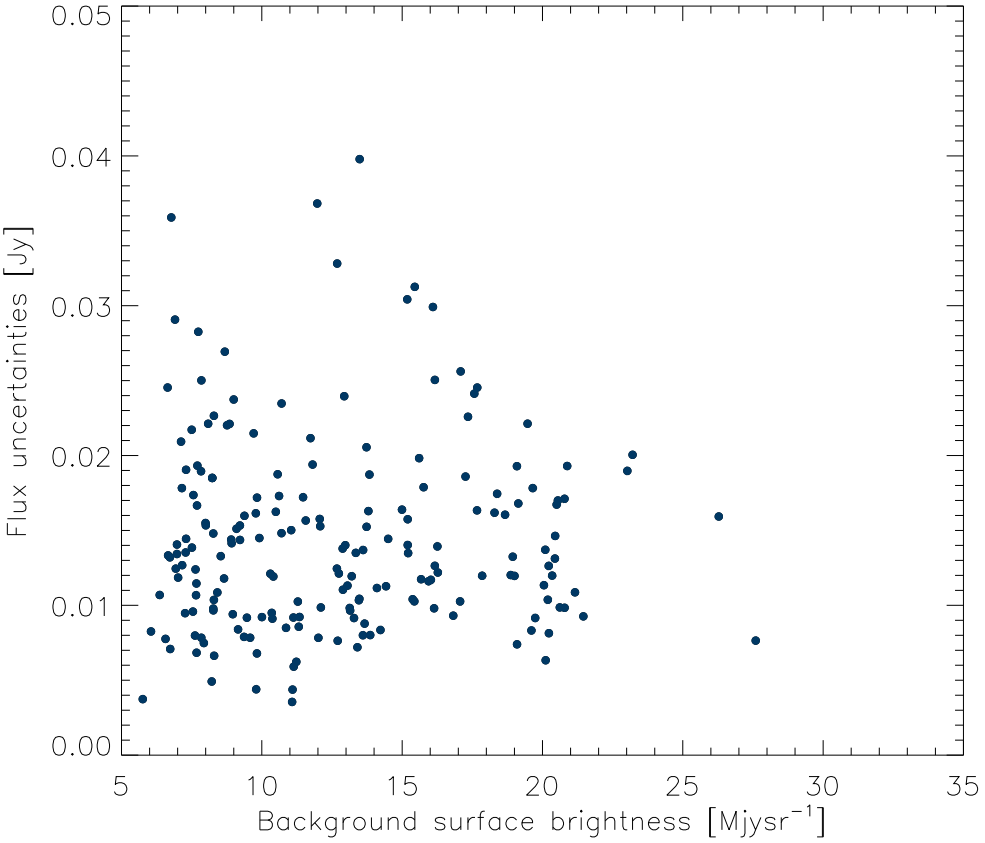


Figure 14: Individual uncertainties versus the background surface brightness

# References


del Burgo, C. et al., Proceedings of the Conference Exploiting the ISO Data Archive. Infrared Astronomy in the Internet Age, in Siguenza, Spain 24-27 June, 2002. Edited by C. Gry et al. To be published as ESA Publications Series, ESA SP-511

Gabriel C., 1997, in Proc. of the ADASS VI conference (Eds.: G. Hunt, H.E. Payne, ASP Conf.Ser. 125), 108

Heinrichsen, I., Walker, H.J., Klass, U., Sylvester, R.J., Lemke, D., 1999, MNRAS, 304, 589

Herbstmeier, U., 1998, ”ISOPHOT Footprint Tables Explanatory Supplement”

Holland, W. S., et al., 1998, Nature, 392, 788

Kiss, Cs., Klaas, U., 2000, ”General Re-validation of Point Source Photometry from PHT22 Mini-Maps”

Richards, P., Klaas, U., ”Report on the Scientific Validation of the mini-map photometry processing in the PHT pipeline (Version 1.0)”

Klaas U. et al., 2002, ”ISOPHOT Calibration Accuracies (Version 5.0)”

Laureijs, R.J., 1999, ”Point spread function fractions related to the ISOPHOT C100 and C200 arrays”, ISO Data Center, Villafranca

Laureijs, R.J., de Muizon, M.J., ”Processing of ISOPHOT chopped photometry at 25 micron”, Internal calibration report, Version 1.0, 31 March 2000

Müller, T.G., Lagerros, J.S.V., 2002, A&A, 381, 324

Plets, A., Vynckier, C., 1999, A&A 343, 496

Walker, H.J., Heinrichsen, I., 2000, Icarus 143, 147

# Appendix A: primary standards provided by Cohen/Hammersley

| HD | HR | Name | Sp | V(J) | VT | B-V |
|---|---|---|---|---|---|---|
| 28 | 3 | 33 Psc | K1III | 4.61 | 4.738 | 1.029 |
| 787 | 37 | IRC-20005 | K5III | 5.29 | 5.445 | 1.478 |
| 1522 | 74 | iot Cet | K1.5III | 3.56 | 3.688 | 1.214 |
| 1879 | 79 | IRC-20008 | M0III | 6.43 | 6.622 | 1.595 |
| 2261 | 99 | alf Phe | K0IIIb | 2.40 | 2.519 | 1.083 |
| 2637 | 117 | 12 Cet | M0III | 5.72 | 5.911 | 1.545 |
| 4128 | 188 | bet Cet | K0III | 2.04 | 2.159 | 1.019 |
| 6805 | 334 | eta Cet | K1.5III | 3.46 | 3.585 | 1.161 |
| 6860 | 337 | bet And | M0III | 2.07 | 2.264 | 1.576 |
| 8512 | 402 | tet Cet | K0III | 3.60 | 3.732 | 1.065 |
| 8810 | 420 | SAO 248381 | K5III | 5.92 | 6.093 | 1.561 |
| 11353 | 539 | zet Cet | K0III | 3.74 | 3.858 | 1.136 |
| 12524 | 602 | chi Phe | K5III | 5.15 | 5.319 | 1.471 |
| 12929 | 617 | alf Ari | K2IIIab | 2.01 | 2.152 | 1.151 |
| 14641 | 688 | SAO 232717 | K5III | 5.81 | 5.991 | 1.570 |
| 16212 | 759 | 80 Cet | M0III | 5.53 | 5.716 | 1.607 |
| 25025 | 1231 | gam Eri | M0.5III | 2.97 | 3.149 | 1.588 |
| 27697 | 1373 | del01 Tau | K0III | 3.77 | 3.868 | 0.983 |
| 29085 | 1453 | ups01 Eri | K0III | 4.49 | 4.613 | 0.972 |
| 29139 | 1457 | alf Tau | K5III | 0.87 | 1.160 | 1.538 |
| 29291 | 1464 | ups02 Eri | G8IIIa | 3.81 | 3.918 | 0.957 |
| 32887 | 1654 | eps Lep | K5IIIv | 3.19 | 3.351 | 1.460 |
| 33872 | 1699 | SAO 195639 | K5III | 6.57 | 6.763 | 1.653 |
| 37160 | 1907 | phi02 Ori | K0IIIb | 4.09 | 4.198 | 0.951 |
| 39853 | 2065 | IRC-10101 | K5III | 5.62 | 5.800 | 1.523 |
| 40035 | 2077 | del Aur | K0III | 3.72 | 3.842 | 1.010 |
| 41047 | 2131 | SAO 196413 | K5III | 5.54 | 5.719 | 1.580 |
| 47105 | 2421 | gam Gem | A0IV | 1.93 | 2.024 | 0.001 |
| 48915 | 2491 | alf CMa | A1V | -1.44 |  | 0.009 |
| 49293 | 2506 | 18 Mon | K0III | 4.48 | 4.598 | 1.099 |
| 61294 | 2935 | IRC+40183 | M0III | 5.77 | 5.952 | 1.654 |
| 62509 | 2990 | bet Gem | K0IIIb | 1.16 | 1.325 | 0.991 |
| 73603 | 3425 | IRC-20172 | K5III | 6.32 | 6.486 | 1.592 |
| 74860 | 3480 | IRC-10205 | K5III | 6.22 | 6.418 | 1.608 |
| 76110 | 3535 | SAO 199737 | M0III | 5.79 | 5.990 | 1.508 |
| 81420 | 3738 | 28 Hya | K5III | 5.60 | 5.757 | 1.523 |
| 81797 | 3748 | alf Hya | K3II-III | 1.99 | 2.161 | 1.440 |
| 82660 | 3802 | IRC-10220 | K5III | 5.95 | 6.125 | 1.501 |
| 82668 | 3803 | N Vel | K5III | 3.16 | 3.346 | 1.538 |
| 89998 | 4080 | r Vel | K1III | 4.82 | 4.943 | 1.095 |
| 92305 | 4174 | gam Cha | K5III | 4.11 | 4.283 | 1.580 |
| 95272 | 4287 | alf Crt | K1III | 4.08 | 4.205 | 1.079 |
| 95314 | 4289 | IRC-10247 | K5III | 5.86 | 6.024 | 1.501 |
| 95578 | 4299 | 61 Leo | M0III | 4.73 | 4.910 | 1.593 |
| 96833 | 4335 | psi UMa | K1III | 3.00 | 3.128 | 1.144 |

Table 2: List of ISOPHOT primary standards (see in Sect. 2). The stars which were actually used for ISOPHOT calibration are underlined

| HD | HR | Name | Sp | V(J) | VT | B-V |
|---|---|---|---|---|---|---|
| 101666 | 4503 | IRC-30181 | K5III | 5.20 | 5.380 | 1.475 |
| 102461 | 4526 | SAO 239373 | K5III | 5.42 | 5.617 | 1.664 |
| 108225 | 4728 | 6 CVn | G9III | 5.01 | 5.119 | 0.955 |
| 108903 | 4763 | gam Cru | M3.5III | 1.59 | 1.832 | 1.600 |
| 109615 | | SAO 63089 | A0V | 7.28 | 7.269 | -0.024 |
| 110458 | 4831 | w Cen | K0III | 4.66 | 4.783 | 1.075 |
| 111812 | 4883 | 31 Com | G0IIIp | 4.93 | 5.001 | 0.681 |
| 111996 | | SAO 63234 | K1V | 9.46 | 9.566 | 1.080 |
| 112213 | 4906 | SAO 223760 | M0III | 5.46 | 5.653 | 1.668 |
| 113996 | 4954 | 41 Com | K5III | 4.80 | 4.955 | 1.482 |
| 114710 | 4983 | bet Com | F9.5V | 4.23 | 4.311 | 0.572 |
| 115968 | | SAO 63483 | G8III | 8.01 | 8.085 | 0.708 |
| 116405 | | SAO 44585 | A0V | 8.34 | 8.335 -0.074 | |
| 116842 | 5062 | 80 UMa | A5V | 3.99 | 4.023 | 0.169 |
| 116870 | 5064 | 68 Vir | M0IIIv | 5.27 | 5.431 | 1.477 |
| 119193 | 5152 | SAO 241098 | M0III | 6.43 | 6.625 | 1.671 |
| 120477 | 5200 | ups Boo | K5.5III | 4.05 | 4.216 | 1.520 |
| 120787 | 5213 | SAO 16186 | G3V | 5.97 | 6.070 | 0.974 |
| 121131 | | SAO 83052 | K1V | 8.37 | 8.446 | 0.815 |
| 123139 | 5288 | tet Cen | K0IIIb | 2.06 | 2.190 | 1.011 |
| 123977 | 5302 | SAO 29019 | K0III | 6.47 | 6.582 | 1.023 |
| 123999 | 5304 | 12 Boo | F9IVw | 4.82 | 4.875 | 0.541 |
| 124897 | 5340 | alf Boo | K1.5III | -0.05 | 0.286 | 1.239 |
| 125161 | 5350 | iot Boo | A9V | 4.75 | 4.772 | 0.236 |
| 126927 | 5410 | 106 Vir | K5III | 5.42 | 5.593 | 1.490 |
| 127243 | 5420 | 24 Boo | G3IV | 5.58 | 5.677 | 0.864 |
| 127334 | 5423 | SAO 45075 | G5V | 6.36 | 6.438 | 0.702 |
| 127665 | 5429 | rho Boo | K3III | 3.57 | 3.722 | 1.298 |
| 128000 | 5442 | IRC+60228 | K5III | 5.74 | 5.902 | 1.529 |
| 128167 | 5447 | sig Boo | F2V | 4.47 | 4.513 | 0.364 |
| 130157 | 5513 | IRC-20268 | K5III | 6.05 | 6.242 | 1.649 |
| 132142 | | SAO 29336 | K1V | 7.77 | 7.829 | 0.785 |
| 132833 | 5590 | IRC+00257 | M0III | 5.52 | 5.711 | 1.692 |
| 133208 | 5602 | bet Boo | G8IIIa | 3.49 | 3.588 | 0.956 |
| 133550 | 5615 | SAO 206292 | K5III | 6.27 | 6.480 | 1.658 |
| 133774 | 5622 | nu Lib | K5III | 5.19 | 5.372 | 1.589 |
| 134493 | 5648 | SAO 29420 | K0III | 6.33 | 6.442 | 1.050 |
| 136422 | 5705 | phi01 Lup | K5III | 3.57 | 3.745 | 1.534 |
| 137744 | 5743 | zet01 Lib | K5III | 5.64 | 5.821 | 1.545 |
| 138265 | 5755 | IRC+60234 | K5III | 5.90 | 6.072 | 1.441 |
| 138481 | 5763 | nu01 Boo | K5III | 5.04 | 5.222 | 1.589 |
| 139127 | 5797 | ome Lup | K4.5III | 4.34 | 4.506 | 1.412 |
| 139669 | 5826 | tet Umi | K5III | 5.00 | 5.168 | 1.545 |
| 139798 | 5830 | SAO 45650 | F2V | 5.76 | 5.797 | 0.353 |
| 141653 | 5886 | SAO 16848 | A2IV | 5.19 | 5.200 | 0.062 |
| 142091 | 5901 | kap CrB | K1IVa | 4.79 | 4.919 | 0.996 |

Table 2: List of ISOPHOT primary standards (see in Sect. 2 cont.)

| HD | HR | Name | Sp | V(J) | VT | B-V |
|---|---|---|---|---|---|---|
| 142373 | 5914 | chi Her | F8Ve... | 4.60 | 4.672 | 0.563 |
| 142574 | 5924 | IRC+20288 | M0III | 5.45 | 5.627 | 1.588 |
| 143435 | 5957 | IRC+40277 | K5III | 5.61 | 5.772 | 1.529 |
| 144204 | 5981 | IRC+50247 | K5III | 5.93 | 6.085 | 1.498 |
| 144284 | 5986 | tet Dra | F8IV | 4.01 | 4.064 | 0.528 |
| 144579 | | SAO 65065 | G8V | 6.66 | 6.741 | 0.734 |
| 146051 | 6056 | del Oph | M0.5III | 2.73 | 2.919 | 1.584 |
| 148387 | 6132 | eta Dra | G8IIIb | 2.73 | 2.831 | 0.910 |
| 151249 | 6229 | eta Ara | K5III | 3.77 | 3.949 | 1.562 |
| 156277 | 6417 | zet Aps | K1III | 4.76 | 4.899 | 1.194 |
| 156729 | 6436 | 69 Her | A2V | 4.64 | 4.628 | 0.043 |
| 157325 | 6464 | 74 Her | M0III | 5.51 | 5.684 | 1.586 |
| 158485 | 6514 | SAO 30387 | A4V | 6.49 | 6.510 | 0.139 |
| 163376 | 6682 | SAO 228578 | M0III | 4.88 | 5.075 | 1.617 |
| 163588 | 6688 | ksi Dra | K2III | 3.73 | 3.867 | 1.177 |
| 163770 | 6695 | tet Her | K1IIa | 3.86 | 3.996 | 1.350 |
| 164058 | 6705 | gam Dra | K5III | 2.24 | 2.413 | 1.521 |
| 167042 | 6817 | SAO 30784 | K1III | 5.97 | 6.074 | 0.943 |
| 168009 | 6847 | SAO 47343 | G2V | 6.30 | 6.373 | 0.641 |
| 168723 | 6869 | eta Ser | K0III-IV | 3.23 | 3.352 | 0.941 |
| 169916 | 6913 | lam Sgr | K1IIIb | 2.82 | 2.945 | 1.025 |
| 172167 | 7001 | alf Lyr | A0V | 0.03 | -0.001 | |
| 172323 | | SAO 17936 | F9V | 8.10 | 8.153 | 0.564 |
| 174387 | 7092 | SAO 229336 | M0III | 5.51 | 5.696 | 1.641 |
| 175775 | 7150 | ksi02 Sgr | K1III | 3.52 | 3.656 | 1.151 |
| 176524 | 7180 | ups Dra | K0III | 4.82 | 4.949 | 1.151 |
| 177716 | 7237 | tau Sgr | K1IIIb | 3.32 | 3.448 | 1.169 |
| 178345 | 7259 | bet CrA | K0II | 4.10 | 4.244 | 1.163 |
| 180711 | 7310 | del Dra | G9III | 3.07 | 3.188 | 0.990 |
| 181109 | 7323 | IRC-30409 | M0III | 6.56 | 6.750 | 1.680 |
| 181276 | 7328 | kap Cyg | G9III | 3.80 | 3.900 | 0.950 |
| 181597 | 7341 | SAO 48315 | K1III | 6.32 | 6.445 | 1.123 |
| 184400 | | SAO 48555 | F5 | 8.51 | 8.552 | 0.460 |
| 184467 | | SAO 31745 | K2V | 6.60 | 6.710 | 0.859 |
| 184960 | 7451 | SAO 31782 | F7V | 5.71 | 5.775 | 0.475 |
| 185395 | 7469 | tet Cyg | F4V | 4.49 | 4.543 | 0.395 |
| 186427 | 7504 | 16 Cyg B | G2.5V | 6.25 | 6.286 | 0.661 |
| 187150 | 7525 | IRC-10522 | K5III | 6.47 | 6.677 | 1.676 |
| 187642 | 7557 | alf Aql | A7V | 0.76 | 0.955 | 0.221 |
| 187660 | 7559 | IRC+00454 | K5III | 6.12 | 6.305 | 1.573 |
| 188154 | 7584 | 56 Aql | K5III | 5.76 | 5.967 | 1.664 |
| 189276 | 7633 | IRC+60274 | K4.5IIIa | 4.98 | 5.153 | 1.584 |
| 189831 | 7652 | SAO 211767 | K5III | 4.77 | 4.924 | 1.417 |
| 190056 | 7659 | IRC-30424 | K1III | 4.99 | 5.135 | 1.208 |
| 191277 | 7701 | 66 Dra | K3III | 5.40 | 5.542 | 1.191 |
| 192781 | 7742 | IRC+60284 | K5III | 5.81 | 5.975 | 1.476 |

Table 2: List of ISOPHOT primary standards (see in Sect. 2 cont.).

| HD | HR | Name | Sp | V(J) | VT | B-V |
|---|---|---|---|---|---|---|
| 195820 | 7854 | SAO 32649 | K0III | 6.20 | 6.324 | 1.018 |
| 196171 | 7869 | alf Ind | K0III | 3.11 | 3.221 | 0.998 |
| 196321 | 7873 | 70 Aql | K5II | 4.91 | 5.076 | 1.606 |
| 196917 | 7909 | IRC-30434 | M0III | 5.75 | 5.940 | 1.551 |
| 197345 | 7924 | alf Cyg | A2Iae | 1.25 | 1.343 | 0.092 |
| 198048 | 7952 | zet Ind | K5III | 4.90 | 5.066 | 1.494 |
| 198149 | 7957 | eta Cep | K0IV | 3.41 | 3.525 | 0.912 |
| 198542 | 7980 | ome Cap | M0III | 4.12 | 4.300 | 1.633 |
| 199345 | 8015 | 7 Aqr | K5III | 5.49 | 5.658 | 1.474 |
| 200914 | 8080 | 24 Cap | M0.5III | 4.49 | 4.703 | 1.604 |
| 216032 | 8679 | tau02 Aqr | M0III | 4.05 | 4.222 | 1.570 |
| 216131 | 8684 | mu Peg | G8III | 3.51 | 3.610 | 0.933 |
| 216149 | 8685 | SAO 214134 | M0III | 5.43 | 5.570 | 1.444 |
| 217902 | 8774 | kap Gru | K5III | 5.37 | 5.542 | 1.453 |
| 217906 | 8775 | bet Peg | M2.5II-III | 2.44 | 2.659 | 1.655 |
| 218670 | 8820 | iot Gru | K1III | 3.88 | 3.995 | 0.998 |
| 219449 | 8841 | psi01 Aqr | K0III | 4.24 | 4.362 | 1.107 |
| 219784 | 8863 | gam Scl | K1III | 4.41 | 4.535 | 1.109 |
| 220440 | 8898 | SAO 247858 | M0III | 5.75 | 5.927 | 1.611 |
| 224630 | 9073 | IRC-30472 | K5III | 5.59 | 5.779 | 1.599 |

Table 2: List of ISOPHOT primary standards (see in Sect. 2 cont.).

# Appendix B: description of the catalogue

| Column | Field | Unit | Format | Description |
|---|---|---|---|---|
| (1) | Object name | | | SIMBAD compatible name. Filled if a compact source from SIMBAD can be associated with the ISOPHOT target without doubt. |
| (2) | Object type | | | Standard SIMBAD code for object type |
| (3) | ISO name | | | Object name given by the ISO observer |
| (4) | TDTNUM_ON | | | The 8-digit TDTNUM of the on-source observation |
| (5) | On_ Meas. | | | Index of the on-source measurement within TDTNUM_ ON |
| (6) | RA(2000) | | | Right ascension, hours |
| (7) | Dec(2000) | | | Declination, degrees |
| (8) | Detector | | | ISOPHOT detector (P1, P2, P3, C100, or C200) |
| (9) | Wavelength | [micron] | | Nominal wavelength of the ISOPHOT filter |
| (10) | Aperture | [arcsec] | | Circular for P1,P2,P3, square for C100 and C200 detectors |
| (11) | Epoch | | | Epoch of the observation |
| (12) | TDTNUM_ OFF | | | The 8-digit TDTNUM of the off-source observation |
| (13) | Off_Meas. | | | Index of the off-source measurement within TDTNUM_OFF |
| (14) | Flux density | [Jy] | | Flux density of the source. In case of a point source the measured flux is corrected for the size of the point spread function. In case of an extended source it corresponds to the integrated brightness. No colour correction applied. |
| (15) | Flux uncertainty | [Jy] | | Flux uncertainty. No colour correction applied. |
| (16) | Background | [MJy/sr] | | Background surface brightness. No colour correction applied. |
| (17) | Detection | [sigma] | | The significance level of the source being detected above the background. |
| (18) | Object size | | | Indicates if the object is point-like (P) or extended (E) |
| (19) | Quality | | | Quality of the observation<br>R1 – Standard processing according to the scheme described in the report.<br>R2 – Minimap performed in astronomical (rather than satellite) coordinate<br>R3 – ISOPHOT position differs from SIMBAD position by more than 10”<br>R4 – Suspected ISO pointing problem<br>R5 – Only one FCS is available<br>R6 – No useful FCS is available, default FCS is used<br>R7 – Archive quality mark<br>R8 – Not enough data points to perform drift correction<br>R9 – Fitting smooth baseline to the data points failed, drift correction (partly/completely) omitted<br>R10 – Observation was carried out at the very end of orbit. Reduced photometric reliability at orbital phase greater than 0.8<br>R11 – A large increase in the proton flux from the Sun was observed<br>R12 – Non-stabilised target signal<br>R13 – Measured flux was out of the empirically calibrated range |

Table 3: